ACSNANO
www.acsnano.org
ARTICLE

High-Performance Transition Metal Phosphide Alloy Catalyst for Oxygen Evolution Reaction

Kewei Liu,[†,⊥] Changlin Zhang,[‡,§,⊥] Yuandong Sun,[†] Guanghui Zhang,[∥] Xiaochen Shen,[‡] Feng Zou,[†] Haichang Zhang,[†] Zhenwei Wu,[∥] Evan C. Wegener,[∥] Clinton J. Taubert,[†] Jeffrey T. Miller,[*,∥] Zhenmeng Peng,[*,‡] and Yu Zhu[*,†]

[†]Department of Polymer Science and [§]Department of Chemical and Biomolecular Engineering, University of Akron, 170 University Circle, Akron, Ohio 44325, United States

[‡]Joint Center for Artificial Photosynthesis, Lawrence Berkeley National Laboratory, Berkeley, California 94720, United States

[∥]School of Chemical Engineering, Purdue University, 480 Stadium Mall Drive, West Lafayette, Indiana 47907, United States

Supporting Information

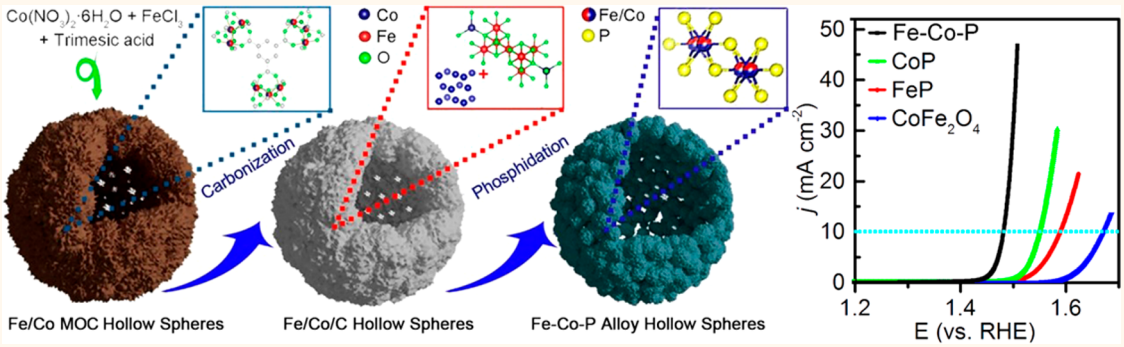

ABSTRACT: **Oxygen evolution reaction (OER) is a pivotal process in many energy conversion and storage techniques, such as water splitting, regenerative fuel cells, and rechargeable metal-air batteries. The synthesis of stable, efficient, non-noble metal-based electrocatalysts for OER has been a long-standing challenge. In this work, a facile and scalable method to synthesize hollow and conductive iron−cobalt phosphide (Fe−Co−P) alloy nanostructures using an Fe−Co metal organic complex as a precursor is described. The Fe−Co−P alloy exhibits excellent OER activity with a specific current density of 10 mA/cm^2 being achieved at an overpotential as low as 252 mV. The current density at 1.5 V (*vs* reversible hydrogen electrode) of the Fe−Co−P catalyst is 30.7 mA/cm^2, which is more than 3 orders of magnitude greater than that obtained with state-of-the-art Fe−Co oxide catalysts. Our mechanistic experiments and theoretical analysis suggest that the electrochemical-induced high-valent iron stabilizes the cobalt in a low-valent state, leading to the simultaneous enhancement of activity and stability of the OER catalyst.**

KEYWORDS: *Fe−Co−P alloy, self-assembly, hollow sphere, XANES, EXAFS, oxygen evolution reaction*

Oxygen evolution reaction (OER) has received great research interest in recent years toward the implementation of energy conversion and storage techniques, such as photoelectrolytic/electrolytic water splitting, regenerative fuel cells, and rechargeable metal-air batteries.[1−7] Due to the sluggish reaction kinetics of OER, large amounts of noble metal oxides (*e.g.*, IrO_2 and RuO_2) are required to overcome the activation energy barriers of O−H bond breaking and O−O bond formation.[8,9] It has been one of the more longstanding challenges to reduce or even eliminate the use of noble metals in OER, especially when the activity, stability, cost-effectiveness, and environmental benignity are considered in evaluating the proposed alternative catalyst.[10−17] Hence, the development of a low-cost, stable OER catalyst without sacrificing catalytic performance is crucial. Great progress has been achieved in the past decade in exploring new OER catalysts as alternatives to IrO_2 and RuO_2.[18,19] Various metal oxides, including cobalt oxides,[20−23] manganese oxides,[24−26] Ni−Fe oxides,[27] Ni−Co oxides,[28,29] Ni−Fe−Co oxides,[30] and others,[31] were synthesized and investigated as catalysts to OERs. Metal hydroxides/oxyhydroxides, such as nickel hydride,[32] nickel−cobalt double hydroxide,[33] cobalt−chromium double hydroxide,[34] nickel−vanadium double hydroxide,[35] and cobalt oxyhydroxide,[36] have been intensively studied for their attractive OER performance. Koper and

Received: July 3, 2017
Accepted: December 6, 2017
Published: December 6, 2017

DOI: 10.1021/acsnano.7b04646
ACS Nano XXXX, XXX, XXX−XXX

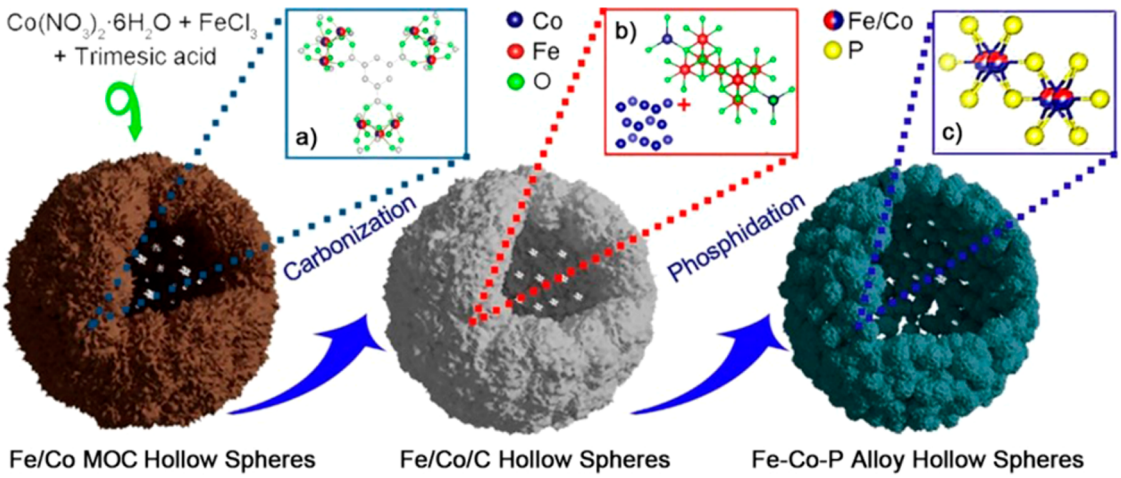

Figure 1. Schematic illustration of hollow Fe−Co−P alloy material synthesis. The Fe−Co MOC was prepared *via* a hydrothermal reaction with $Co(NO_3)_2{\cdot}6H_2O$ and $FeCl_3$ as the metal sources and trimesic acid as the ligand. The trimesic molecule was coordinated with Co or Fe ions to form a metal organic complex structure (inset a). Fe−Co oxide/C hollow spheres were obtained after carbonization at 500 °C in Ar. A mixture of $CoFe_2O_4$ and Co was observed in the Fe−Co oxide/C hollow spheres (inset b). A Fe−Co−P alloy nanostructure was obtained after a controlled phosphidation by *in situ*-generated PH_3. The crystal structure of the Fe−Co−P alloy is presented in inset c.

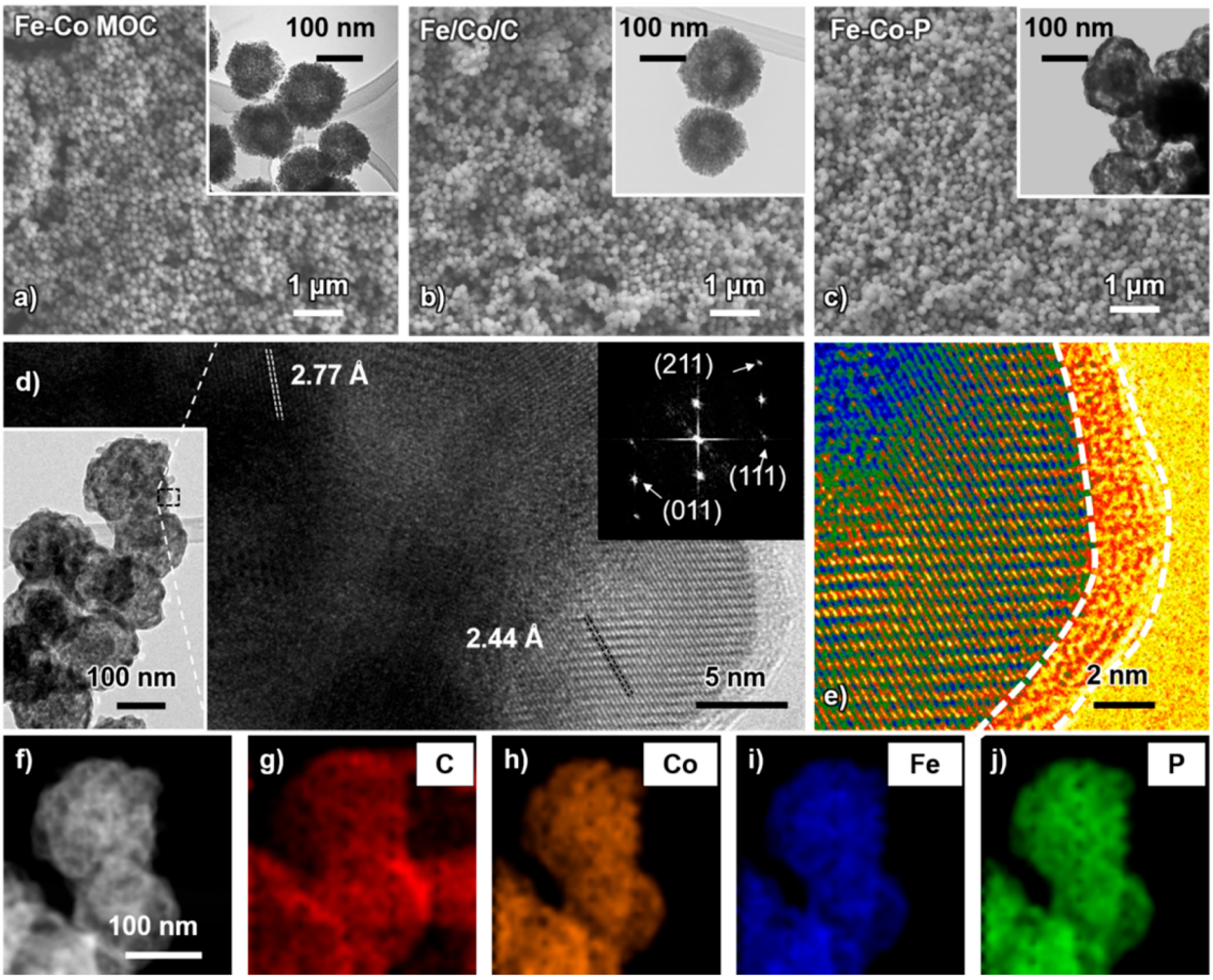

Figure 2. Morphology and elemental distribution of the Fe−Co−P nanostructures. (a−c) Scanning electron microscopy images (inset: TEM images) of the prepared Fe−Co MOC, $CoFe_2O_4$-based metal oxide/C composites, and Fe−Co−P nanostructure. (d) High-resolution TEM image of the Fe−Co−P nanostructure with a corresponding fast Fourier transform pattern. (e) Colored *Z*-contrast HRTEM image of the Fe−Co−P nanostructure. (f) Scanning TEM image and the corresponding elemental mapping of (g) carbon, (h) cobalt, (i) iron, and (j) phosphorus.

DOI: 10.1021/acsnano.7b04646
ACS Nano XXXX, XXX, XXX−XXX

colleagues showed that Ni−Fe and Ni−Mn double hydroxides can be promising OER catalysts based on a joint theoretical−experimental study.[37] Bell and co-workers mechanistically revealed the origin of pronounced OER activities of Ni−Fe-based oxyhydroxides.[38] Due to the low intrinsic electrical conductivity, metal oxide/hydroxide/oxyhydroxide materials have high charge transfer resistance, resulting in large overpotentials.[39,40] Hybridization with various carbonaceous materials, such as graphene,[41,42] heteroatom-doped graphene, carbon nanotube,[43,44] and porous carbon nanosheets,[45] have been explored. More recently, metal sulfides and nitrides with better intrinsic electrical conductivity have been investigated. Zhang's group fabricated Co−S nanosheets on carbon tubes embedded on carbon paper, which exhibited comparable overpotentials to benchmark RuO_2.[46] In another work, Ni_3N nanosheets were employed as an efficient OER catalyst due to their metallic nature and disordered structure.[47] The structural stability of carbon-hybridized materials and metal sulfides or nitride nanosheets in OERs are still challenging,[48] which hinders their implementation in OER-related applications. Emerging phosphide[49−51] compounds exhibit the most interesting OER performance (*i.e.*, superior electrochemical activity, long-term stability, and low cost); however, the OER mechanism of phosphide compounds remains unknown due to their complicated compositions.

In this work, a facile and scalable method for preparing hollow and conductive Fe−Co−P alloys with outstanding OER catalytic properties is reported. The hollow structure provides abundant active surface sites and short mass transfer pathways. The metallic conductivity facilitates charge transfer, and the uniform structure enables the structure−properties relationship investigation. This general approach of designing multifunctional alloy OER catalysts could be applied in a variety of related research topics, such as fuel cells, electrolyzers, and metal-air batteries.

RESULTS AND DISCUSSION

Synthesis of Fe−Co−P Alloy Materials. A schematic illustration for the preparation of the Fe−Co−P catalyst is displayed in Figure 1. The Fe−Co metal−organic complex (MOC) was prepared by a hydrothermal reaction. To prepare the initial Fe−Co MOC, iron chloride ($FeCl_3$) and cobalt nitrate ($Co(NO_3)_2{\cdot}6H_2O$) with a stoichiometric ratio of 3:2 were dissolved in a solvent mixture of *N*,*N*-dimethylformamide, ethanol, and water with trimesic acid (BTC) as the ligand. The mixture was heated at 150 °C for 12 h, allowing the formation of an Fe−Co MOC structure through a self-assembly process (Figure 1a). The Fe−Co MOC was then annealed at 500 °C in Ar with a ramp rate of 2 °C/min. The organic ligands were carbonized, and metal (Fe/Co) oxides were formed. Sodium hypophosphite (NaH_2PO_2) was used as the phosphorus (P) source due to its low toxicity. Upon heating, NaH_2PO_2 thermally decomposed and released PH_3, which converted the metal oxide/C structure into an Fe−Co−P alloy.[52] No surfactant or template was applied in the entire process, which avoided labor-intensive post-treatment and enabled a cost-effective scale-up.

Characterization of Fe−Co−P Alloy Materials. The precursor Fe−Co MOC materials and their carbonization and phosphidation products were characterized. The scanning electron microscopy (SEM) imaging in Figure 2a shows that the Fe−Co MOC structure assembles into highly uniform nanospheres. The transmission electron microscopy (TEM) image in the inset revealed the hollow cavities of Fe−Co MOC as evidenced by the obvious contrast difference. The details of the structure evolution are illustrated in Figure S1. During the hydrothermal reaction, the iron and cobalt metal ions coordinated with trimesic acid and formed small clusters in the first 6 h of reaction. Followed by another 3 h reaction, the clusters aggregated into the solid spheres, as shown in Figure S1b. The formation of the bigger particles could be explained as the Ostwald ripening process. At the same time, the materials within the particle recrystallized under hydrothermal condition. The crystallized materials were formed on the surface of the particle, resulting in a hollow spherical hierarchical structure. Such a dissolution/crystallization process has been reported previously in our report.[53] The carbonization of Fe−Co MOC was also studied by thermogravimetric analysis (TGA) over a temperature range from room temperature to 800 °C, which revealed that there were several weight loss steps, as shown in Figure S2. The annealing temperature (500 °C) ensured carbonization without causing further degradation. After carbonization, the hollow structure was largely maintained in the metal oxide/C composites (mostly of $CoFe_2O_4$), and no significant structural collapse was observed (Figure 2b). Phosphidation was undertaken following a previously reported procedure;[52] however, the annealing temperature and reaction time were adjusted to achieve an optimized product. After phosphidation, a hollow Fe−Co−P nanostructure was obtained (Figure 2c). High-resolution TEM (HRTEM) images in Figure 2d showed *d*-spacings of 2.44 and 2.77 Å, which can be indexed to the interplane of (111) and (011) of the Fe−Co−P alloy, corresponding to the fast Fourier transform (FFT) pattern. The values of the *d*-spacing were between those of FeP and CoP, suggesting an alloy formation of nanostructured Fe−Co−P. The carbon matrix, which improved electric conductivity, was not only characterized by Raman spectroscopy (Figure S3) but also observed and visualized in a colored HRTEM image (Figure 2e). A scanning transmission electron microscopy (STEM) image of the Fe−Co−P alloy (Figure 2f) further confirmed the presence of a highly porous hollow sphere structure. The elemental maps of carbon, iron, cobalt, and phosphorus were also measured by STEM energy-dispersive X-ray spectroscopy (EDX), which demonstrated that all of the elements were homogeneously distributed in the Fe−Co−P alloy nanostructures. The specific surface areas of Fe−Co MOC, Fe/Co/C and Fe−Co−P alloy were determined through the Brunauer−Emmett−Teller (BET) method (Figure S4). The Fe−Co MOC showed a specific surface area of 157.7 m^2/g. After carbonization, the specific surface area of Fe/Co/C was 62.1 m^2/g. It is worth noting that the specific surface area of Fe−Co−P alloy increased to 104.1 m^2/g after phosphidation, which increased the catalytic sites for the oxygen evolution reaction. The Fe−Co−P alloy samples with different Fe/Co ratio were synthesized (Figure S5) as well to explore the optimized composition for OER catalysts.

The structure of the as-prepared materials was investigated by X-ray diffraction (XRD) and analysis of the diffraction patterns (Figure 3). After carbonization at 500 °C, the organic ligand decomposed, as evidenced by the infrared spectrum in Figure S6. Several characteristic peaks related to metal oxides emerged in the XRD results (Figure 3a), which can be attributed to the formation of the spinel structure of $CoFe_2O_4$. Small peaks, related to metallic Co, were also detected in Figure 3a, which may have been formed by carbon-reduced cobalt oxide at 500 °C. Phosphidation was conducted after the

DOI: 10.1021/acsnano.7b04646
ACS Nano XXXX, XXX, XXX−XXX

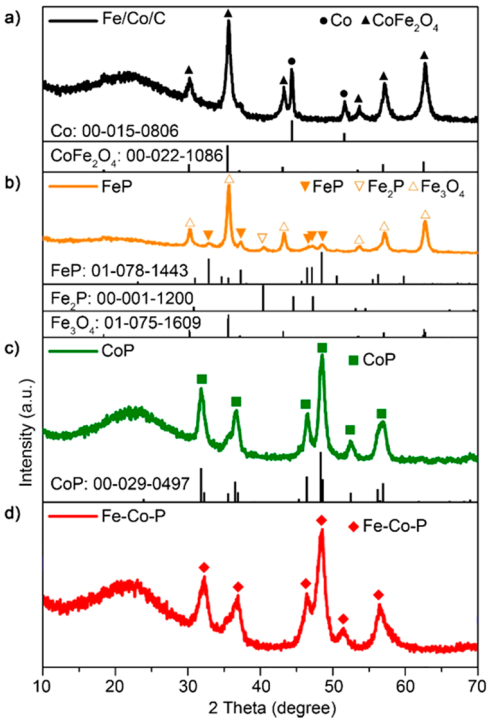

Figure 3. Powder X-ray diffraction profiles of as-prepared $CoFe_2O_4$ (with residual Co), FeP, CoP, and Fe−Co−P. (a) $CoFe_2O_4$ (with Co), (b) FeP, (c) CoP, and (d) fresh Fe−Co−P. During carbonization, the Fe−Co MOC was converted to a mixture of metal oxide/metal ($CoFe_2O_4$ and Co metal). After phosphidation at 400 °C, Co MOC was fully converted to CoP and Fe MOC was partially phosphorized.

carbonization. Before analyzing the complicated ternary Fe−Co−P alloy, FeP and CoP were studied individually. The single metal phosphides, FeP and CoP, were prepared by the same phosphidation procedures with the exception of using only an Fe or Co precursor. Figure 3b shows the phosphidation results of the Fe-MOC-derived materials, which indicate that partial phosphidation was achieved with Fe_3O_4, Fe_2P, and FeP coexisting. The dominant peaks belong to Fe_3O_4. The scattered peaks at 32.7, 37.2, 46.3, 46.9, and 48.3° can be assigned to the (011), (111), (112), (202), and (211) planes of FeP (JCPDS No. 01-078-1443), respectively. Unlike Fe MOC, Co MOC was successfully converted into pure CoP under the same reaction conditions. As can be seen in Figure 3c, the peaks at 31.6, 36.3, 46.4, 48.5, 52.4, and 56.8° are attributed to the (011), (111), (211), (103), and (321) planes of CoP (JCPDS No. 00-029-0497), respectively. No oxides or other cobalt phosphides (*i.e.*, Co_2P, CoP_2, and CoP_3) were observed in Figure 3c, suggesting that Co MOC was fully converted to CoP. The phosphidation product of $CoFe_2O_4$ is shown in Figure 3d. XRD peaks of Fe−Co−P obtained from phosphidation at 400 °C showed the same pattern as that of the CoP with the exception that they are located between the references peaks of FeP and CoP, with the peak positions at 32.2, 36.9, and 51.3° corresponding to the (011), (111), and (103) planes of Fe−Co−P, respectively. The theoretical peak positions of the Fe−Co−P alloy were also calculated by Vegard's law,[54] which was consistent with the experimental results, indicating the as-prepared Fe−Co−P was a uniform alloy. It should be noted that to prepare a uniform metal phosphide, an optimized temperature is crucial both thermodynamically and kinetically. When the phosphidation temperature was set to 350 °C, $CoFe_2O_4$ was partially phosphorized, as shown Figure S7. Peaks attributed to $CoFe_2O_4$ were still observed and accompanied by the formation of the Fe−Co−P alloy. The partially phosphorized sample was also characterized by STEM-EDX (Figure S8). Elemental mappings showed that the phosphorus content on the surface was much higher than that of core parts, suggesting nonuniform phosphorus distribution due to partial phosphidation.

Fe−Co−P Alloy OER Catalyst Evaluation. The OER electrocatalytic properties of the prepared Fe−Co−P alloy catalyst, its monometallic counterparts (CoP and FeP), and $CoFe_2O_4$ were measured in N_2-saturated 1 M KOH electrolyte using a rotating disk electrode. In Figure 4a, the Fe−Co−P catalyst demonstrated a much lower onset potential and higher specific current compared to CoP, FeP, and $CoFe_2O_4$, indicating that it has excellent intrinsic OER catalytic activity. Specifically, the overpotential of the Fe−Co−P alloy catalyst required for achieving a specific current density of 10 mA/cm^2 was only 252 mV, which was significantly lower than that of CoP (320 mV), FeP (361 mV), and $CoFe_2O_4$ (443 mV). The overpotentials of Fe−Co−P alloy catalysts with different Fe/Co ratios were compared in Figure S9. The results indicated that Fe and Co with an atomic ratio of 3:2 exhibited the best OER performance. (Under a specific current density of 10 mA/cm^2,

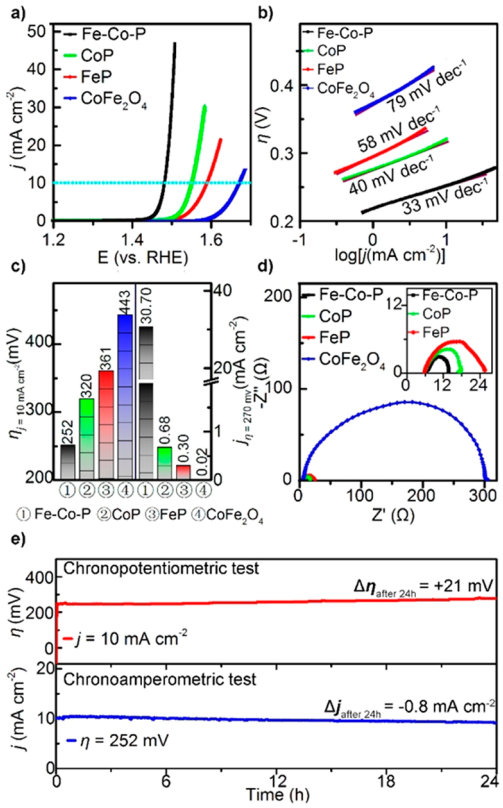

Figure 4. Electrochemical properties of the Fe−Co−P alloy as an OER electrocatalyst. (a) OER polarization curves, (b) Tafel plots, (c) comparison of overpotentials and current densities, and (d) Nyquist plots for the Fe−Co−P alloy, CoP, FeP, and $CoFe_2O_4$ nanostructures. (e) Chronopotentiometric and chronoamperometric tests of the Fe−Co−P alloy catalyst at a constant current density of 10 mA/cm^2 (V−t) and overpotential of 252 mV (i−t), respectively. All the measurements were performed in 1 M KOH with a rotating disk electrode.

DOI: 10.1021/acsnano.7b04646
ACS Nano XXXX, XXX, XXX−XXX

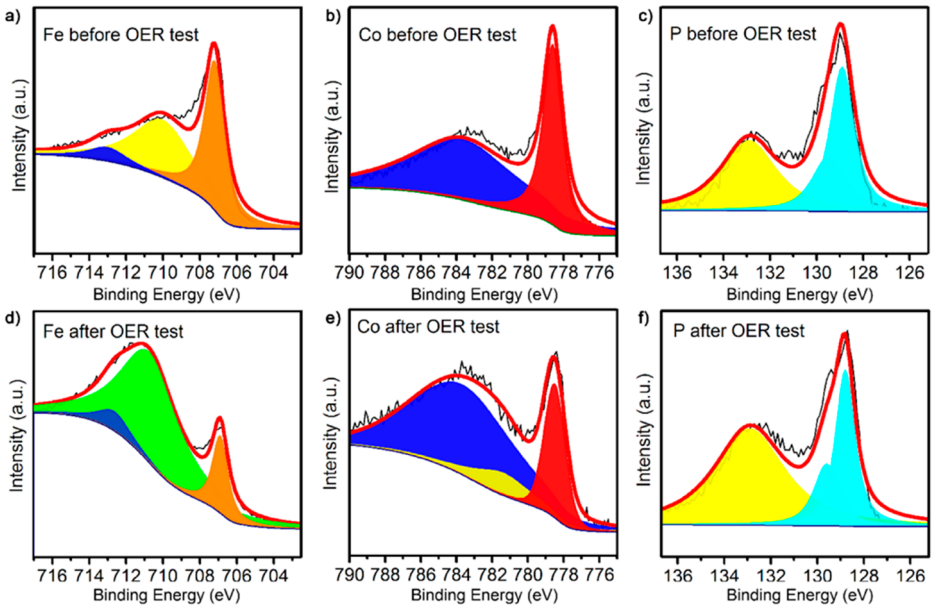

Figure 5. Investigation of the electronic structure of the Fe−Co−P catalyst *via* high-resolution XPS analysis before and after the OER test. (a−c) Fe 2p, Co 2p, and P 2p XPS spectra of the Fe−Co−P alloy catalyst before the OER test. (d−f) Fe 2p, Co 2p, and P 2p XPS spectra of the Fe−Co−P catalyst after the OER test. The Co $2p_{3/2}$ peaks after the OER showed that the valences of Co were similar to those of fresh Fe−Co−P catalyst, indicating the Co elements were stable under the reactions. A peak for FeOOH (green area) was observed, suggestive of an enhanced valence state of Fe after the OER reaction in the Fe 2p XPS spectrum. The black lines in (a−e) are the experimental data. The red lines in (a−e) represent the curve fitting using the Gaussian−Lorentzian algorithm. The orange areas in (a,d), red areas in (b,e), and light blue areas in (c,f) are the metallic peaks for Fe, Co, and P, respectively. The yellow areas in (a,c,e,f) could be associated with oxidation due to air contact. The blue areas in (a,d) and (b,e) are Co and Fe auger peaks.

the overpotentials of Fe−Co−P alloy samples with Fe/Co = 3:1 and Fe/Co = 1:1 were 348 and 303 mV, respectively.) Tafel plots in Figure 4b showed that the Tafel slope for the Fe−Co−P alloy catalyst was 33 mV/dec, confirming the four-electron-transfer reaction pathway.[55] The other catalysts had much higher Tafel slopes with values of 40 mV/dec for CoP, 58 mV/dec for FeP, and 79 mV/dec for $CoFe_2O_4$, indicating a lower conversion efficiency in water oxidation. Remarkably, comparisons of the delivered current density at a specific overpotential of 270 mV (E = 1.50 V *vs* reversible hydrogen electrode, RHE) revealed that the Fe−Co−P alloy catalyst exhibited a value of 30.70 mA/cm^2, which is more than 3 orders of magnitude higher than that of $CoFe_2O_4$ (0.02 mA/cm^2; Figure 4c). Compared to the monometallic phosphides, the Fe−Co−P catalyst also showed greatly improved activity, with current densities ∼100 times higher than that of FeP and 45 times higher than that of CoP. The charge transfer resistances were analyzed by the Nyquist plots in Figure 4d. The solution resistance was consistent for all the measurements with a value of 6 Ω (Figure 4d, inset). The carbonized metal organic complex ($CoFe_2O_4$) showed a much higher interfacial charge transfer resistance of approximately 300 Ω as compared to that of the Fe−Co−P alloy (13 Ω), CoP (18 Ω), and FeP (26 Ω), which is consistent with their OER activities ($CoFe_2O_4$ ≪ FeP < CoP < Fe−Co−P alloy) and signifies the obviously greater reaction kinetics of metal phosphides. The comparison of the OER performance between this Fe−Co−P alloy catalyst and other transition metal phosphide systems are provided in Table SI. The electrochemical stability of the prepared Fe−Co−P catalyst was tested by both chronopotentiometric (V−t) and chronoamperometric (i−t) methods, as shown in Figure 4e. For a constant current output at 10 mA/cm^2, the required overpotential after a 24 h test increased only 21 mV compared to the initial test (252 mV). In the i−t stability test, the retention of current density was 92% (with a loss of only 0.8 mA/cm^2) after a 24 h test. Both measurements suggested that the prepared Fe−Co−P alloy OER catalyst was not only highly active but also very stable in an electrochemical environment. The stabilities of the FeP and CoP catalysts were also tested in Figure S10, in which CoP was active at the beginning but degraded quickly, while FeP was less active but stable throughout. In the first and second CV scans, an irreversible anodic peak was observed at 1.24 V for the Fe−Co−P alloy (Figure S11), which could be associated with the formation of metal oxyhydroxides.[56] Similar irreversible changes were also observed for CoP and FeP but with much higher oxidation potentials at the onset, indicating the modified electronic structure of the Fe−Co−P catalyst caused by the ternary alloy formation.

XPS/XAS Analysis and Simulation. The outstanding OER performance of the Fe−Co−P alloy catalyst benefits from its enhanced intrinsic conductivity. Density of states (DOS) values were calculated to inspect the electronic structure of FeP, CoP, and the Fe−Co−P alloy (Figure S12a). Compared with the DOS of FeP and CoP, the DOS of Fe−Co−P alloy had a higher ratio of states located near the Fermi level, indicating a better conductivity of the ternary alloy. In contrast, the DOS of the other Fe- or Co-containing materials such as $FeCo_2O_4$ (1.194 eV) and FeOOH (1.968 eV) had large band gaps.[57] The crystal structure and model electron density are provided in Figure S12b. To further investigate the local surface changes of the catalyst along with the OER, the Fe−Co−P alloy electrodes were analyzed before and after a reaction by surface-surveying XPS and high-resolution XPS. In the wide range, surface-surveying XPS (Figure S13) detected Fe, Co, P, C, and O peaks. The atomic ratio between Fe and Co was 3:2, which

DOI: 10.1021/acsnano.7b04646
ACS Nano XXXX, XXX, XXX−XXX

was consistent with the stoichiometric ratio between the Fe and Co precursors and suggestive of an accurate control of Fe–Co–P catalyst composition. The appearance of small amounts of oxygen was possibly from either slight oxidation of Fe/Co induced by air exposure or the surface functional OH groups of the carbon layers.[58,59] The carbon peaks were consistent with the HRTEM image (Figure 2e), which showed the formation of amorphous carbon layers. As shown in Figure 5a, the Fe $2p_{3/2}$ at 707.1 eV was observed, which was positively shifted compared to metallic Fe (706.8 eV) while slightly negatively shifted (0.4 eV) compared to pure FeP (707.5 eV).[60] The results could be attributed to the existence of neighboring Co atoms that balance the oxidation state of Fe. In contrast, the Co $2p_{3/2}$ peaks (778.5 eV) in Figure 5b showed a higher binding energy than pure CoP (778.1 eV),[61] indicating electron donation from Co to P and to Fe in the Fe–Co–P alloy system. The peaks with binding energies of 128.8 and 129.5 eV in Figure 5c could be assigned to P $2p_{3/2}$ and P $2p_{1/2}$, which were shifted to lower binding energy positions compared to those of elemental phosphorus, indicating the electron donation from both Fe and Co to P. After OER, a prominent peak on the Fe $2p_{3/2}$ spectrum with a binding energy of 711.1 eV was observed in Figure 5d, which could be associated with the electrochemically formed FeOOH.[62,63] The Co $2p_{3/2}$ peaks after the OER in Figure 5e showed that the valence status of Co was similar to that of the fresh Fe–Co–P catalyst, suggesting that the Co elements were stable under such reactions. Similar results were also observed in other Co/Fe-OOH systems,[56] in which the Fe was believed to be capable of stabilizing the Co species. No obvious peak shits of P 2p were observed after the OER (Figure 5f), indicating the stability of the P element in the catalyst. The yellow peaks in Figure 5a,c,e,f were associated with surface oxidation due to the air exposure. Co and Fe auger peaks were also observed and marked in dark blue (Figure 5a,b,d,e).[56] The electronic structure change of binary alloy catalysts FeP and CoP were also investigated, as shown in Figure S14. For FeP catalyst, the peak related to oxyhydroxide was observed after the OER, which is similar in the case of Fe–Co–P catalyst. Compared with the Co $2p_{3/2}$ peaks in the Fe–Co–P catalyst, clear peak shifts from metallic Co to $Co(OH)_2$ and CoOOH were observed in the CoP catalyst after OER.

Co and Fe K-edge X-ray absorption near-edge structure (XANES) spectra were collected for the Fe–Co–P alloy catalyst before and after OER. As shown in Figure 6a,b, a tiny pre-edge peak (~0.01 in height) of Co(II) is present in $Co(NO_3)_2{\cdot}6H_2O$. For the Fe–Co–P alloy, a much higher peak (~0.2 in height) was observed with an edge energy of 7709 eV, which is the same as that obtained for a Co foil and illustrates the metallic nature of Co in the Fe–Co–P alloy. A broad leading edge peak with a height of ~0.15 (edge energy 7112 eV) was observed in the Fe K-edge data, consistent with the metallic nature of Fe in the Fe–Co–P alloy. After OER (Figure 6b), an increase in the white line intensity (~7725 eV at the Co K-edge and ~7132 eV at the Fe K-edge) of the XANES spectra, as well as a shift in the leading edge to higher energy, was observed for both Co and Fe, suggesting the formation of oxidized species on the catalyst surface. The edge energies of both the Co and Fe edges remain the same as the fresh catalysts, which suggests the bulk of the catalyst remains in the Fe–Co–P alloy.

Co and Fe K-edge extended X-ray absorption fine structure (EXAFS) spectra were also collected for the Fe–Co–P alloy catalyst before and after OER and fitted using modified FeP

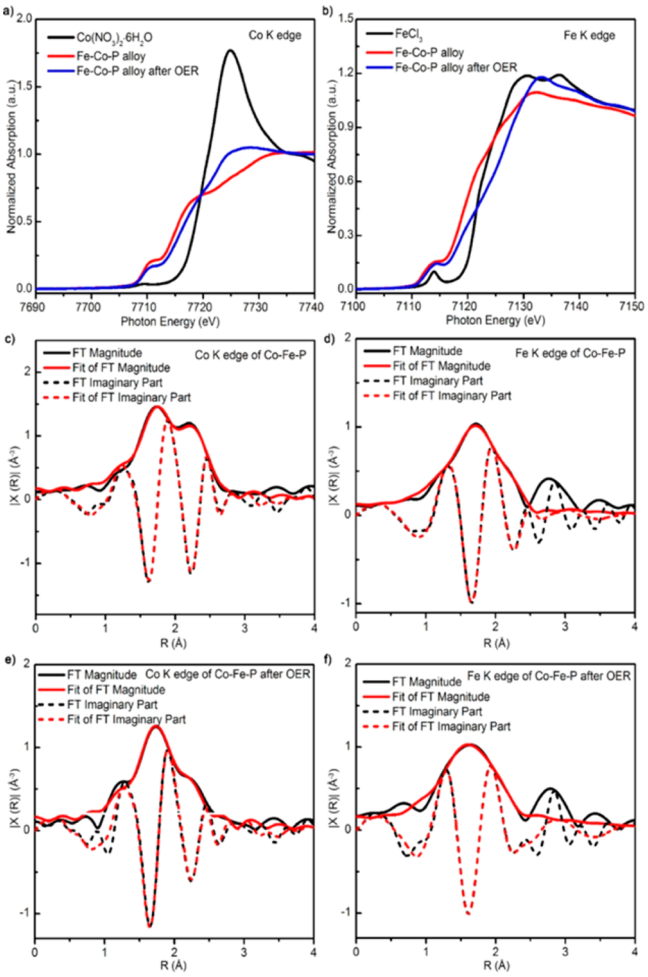

Figure 6. X-ray absorption spectra of the Fe–Co–P catalyst before and after OER. (a,b) XANES spectra at Co K-edges and Fe K-edges of the Fe–Co–P catalyst before OER. (c–f) Fourier transformed k^{-3} weight EXAFS oscillations measured at Co K-edge and Fe K-edge of the Fe–Co–P catalyst before and after OER.

and CoP crystal structures as the models. The fitting results are shown in Figure 6c–f and summarized in Table 1. EXAFS fitting results of the Co K-edge data of the fresh catalyst confirm that the average coordination number of the Co sites is approximately 5 before OER, suggesting the presence of coordinated unsaturated Co sites (CoP has 6 P atoms surrounding each Co). Co–P and Co–Co(Fe) distances are about 2.24 and 2.63 Å, respectively, very similar to the Co–P and Co–Co distances in CoP. EXAFS fitting results of the Fe–Co–P after OER indicate that the average P coordination number of the Co sites did not change much, while the number of Co–Co neighbors decreased from 4 to ~1. The Co–P distance of 2.26 Å is very similar to that of 2.24 Å obtained before OER (within the error). The Co–Co(Fe) distances also did not change. Attempts to include a Co–O path in the fit did not lead to a better data fit, and it is believed that the oxidized Co species represents only a small fraction on the alloy surface, as also suggested by the XANES shift.

EXAFS fitting results of the Fe K-edge data of the fresh catalyst suggest an average P coordination number of 6; the number of Fe neighbors is 2. The Fe–P and Fe–Fe(Co) distances were 2.25 and 2.63 Å, respectively. The Debye–Waller factors of both the Fe–P and Fe–Fe(Co) paths are

DOI: 10.1021/acsnano.7b04646
ACS Nano XXXX, XXX, XXX–XXX

Table 1. Fitting Results Obtained from EXAFS Fe and Co K-Edges of Fe−Co−P Catalyst before and after OER

Fe−Co−P alloy	absorber−scatterer pair	coordination number	bond distance (Å)	σ^2	ΔE_0 (eV)	data range	R factor
before OER Co edge	Co−P	5.0	2.24 ± 0.02	0.008 ± 0.002	−0.9 ± 1.5	k-space 3.0−11.0 Å^{-1}	K^1: 0.003
	Co−Co(Fe)	4.0	2.63 ± 0.01	0.007 ± 0.002		R-space 1.20−2.70 Å	K^2: 0.004
							K^3: 0.007
after OER Co edge	Co−P	5.0	2.26 ± 0.04	0.009 ± 0.002	−3.1 ± 4.7	k-space 3.0−11.0 Å^{-1}	K^1: 0.012
	Co−Co(Fe)	0.9	2.63 ± 0.05	0.001 ± 0.012		R-space 1.27−2.62 Å	K^2: 0.006
							K^3: 0.006
before OER Fe edge	Fe−P	6.0	2.25 ± 0.06	0.014 ± 0.008	−8.8 ± 6.0	k-space 3.0−11.0 Å^{-1}	K^1: 0.003
	Fe−Fe(Co)	2.0	2.63 ± 0.08	0.011 ± 0.011		R-space 1.20−2.46 Å	K^2: 0.003
							K^3: 0.009
after OER Fe edge	Fe−O	2.0	1.96 ± 0.06	0.006 ± 0.011	2.5 ± 3.4	k-space 3.0−10.0 Å^{-1}	K^1: 0.001
	Fe−P	4.0	2.35 ± 0.05	0.016 ± 0.011		R-space 1.00−2.43 Å	K^2: 0.003
							K^3: 0.012

relatively large (0.014 and 0.011), which could also be expected in FeP due to the presence of various Fe−P and Fe−Fe distances. After OER, the presence of Fe−O scattering was observed, which is consistent with the XANES results on the formation of FeOOH species. The average Fe−P distance of 2.35 Å and Fe−O distance of 1.96 ± 0.06 Å were consistent with the Fe−O distances of 1.99−2.12 Å in FeOOH. Consistent with the XANES analysis, the bulk of the alloy remains Fe−Co−P, and the oxidized species were only formed on the surface. The XANES and EXAFS results also reconcile the electrochemistry and XPS analyses, demonstrating that the high-valent state FeOOH is formed on the surface as the major oxidized species. The Co component retained its low-valent nature during the OER reaction with only a small fraction oxidized.

The metal oxyhydroxides were recognized as highly active OER catalysts in many recent studies.[56,64−68] Here, the electrochemistry analysis, quantum calculation, and X-ray analysis suggest that the *in situ*-generated FeOOH on the Fe−Co−P alloy substrates possess highly promising OER-type electrocatalytic properties with the following aspects. (1) The Fe−Co−P phosphides provide metallic conductivity that lowers the required overpotential. Although the pristine metal oxyhydroxide is active for OER, it is not conductive enough to deliver the charge involved in the reactions, while the Fe−Co−P alloy is very conductive. (2) The ternary Fe−Co−P alloy formation could adjust the OH bond breakage and OO bond formation *via* tuning the energetics of all intermediates (*OH, *O, *OOH), in which the adsorptions on a single FeOOH species are too strong, while those on single Co-based sites are too weak. The uniform alloy formation guarantees that the Fe and Co scatters are highly closed, which can provide abundant adjacent active sites. (3) The existence of Fe in the Fe−Co−P alloy can stabilize the Co valence, providing a synergistic effect from the high activity of CoP and high stability of FeP. (4) The carbon outer layer also enables stabilization functionality toward the OER.

CONCLUSION

In conclusion, we present a facile and scalable method for preparing a hollow and conductive Fe−Co−P alloy with outstanding OER catalytic properties. In this material, the hollow structure provides abundant surface active sites and short mass transfer pathways, while the metallic conductivity facilitates charge transfer. Furthermore, the uniform structure enables the investigation of structure/properties relationship. The overpotential of the Fe−Co−P catalyst required for achieving a specific current density of 10 mA/cm^2 is only 252 mV, comparable with noble metal oxide (IrO_2 and RuO_2) catalysts, and superior to most previously reported OER catalysts. The current density at 1.5 V (*vs* RHE) of the Fe−Co−P catalyst was 30.70 mA/cm^2, which is more than 3 orders of magnitude greater than that obtained for $CoFe_2O_4$ (0.02 mA/cm^2), 100 times more active than that of FeP, and 45 times more active than that of CoP. The electrochemically induced high-valent state of Fe stabilized the Co in the low-valent state, enabling the simultaneous enhancement of activity and stability of the OER catalyst. This general approach to designing multifunctional alloy OER catalysts could be applied to a variety of related research topics.

EXPERIMENTAL SECTION

Materials and Characterization. Iron chloride ($FeCl_3$, 98%, Alfa Aesar), cobalt nitrate hexahydrate ($Co(NO_3)_2{\cdot}6H_2O$, 95%, Sigma-Aldrich), trimesic acid (95%, Sigma-Aldich), ethanol (200 proof, Decon Laboratories, Inc.), *N*,*N*-dimethylformamide (DMF, ACS grade, EMD), and sodium hypophosphite monohydrate ($NaH_2PO_2{\cdot}H_2O$, Alfa Aesar) were used as received.

The SEM characterization was carried out using a JEOL JSM-7401F, and TEM images were collected using a JEOL 1203 or FEI Tecnai G2 F20. HRTEM images and corresponding EDX maps were obtained *via* a FEI Tecnai G2 F20 equipped with a super ultrathin window energy-dispersive X-ray spectrometer. XRD patterns were obtained by using a Rigaku Ultima IV X-ray diffractometer with a Cu Kα radiation (λ = 1.5604 Å). The BET method was used to determine the specific surface area in the relative vapor pressure range of 0.001 to 0.27. TGA measurements were carried out by using a Q500 (TA Instruments) under Ar with a temperature ramp of 5 °C/min. The electrochemical analyses were performed by using a CHI760D electrochemical analyzer. Diffuse reflectance infrared Fourier transform spectra (Thermo Scientific) were obtained by log(1/ISB), where the ISB was the IR single beam intensity of the samples.

Fe−Co MOC synthesis. Fe−Co MOC was synthesized *via* a hydrothermal reaction. Specifically, 0.05 g of $FeCl_3$, 0.05 g of $Co(NO_3)_2{\cdot}6H_2O$, and 0.1 g of trimesic acid were dissolved in a mixture of 10 mL of DI water, 10 mL of ethanol, and 10 mL of DMF under vigorous stirring. The solution was then transferred into a Teflon-lined autoclave and heated to 150 °C for 12 h. The final products were centrifuged at 4000 rpm for 20 min and washed three times with ethanol and water. The precipitate was collected and dried at 80 °C. Fe/Co MOC was prepared by dissolving 0.1 g of $FeCl_3$ or 0.1 g of $Co(NO_3)_2{\cdot}6H_2O$ with 0.1 g of trimesic acid in a mixture of 10 mL of DI water, 10 mL of ethanol, and 10 mL of DMF following the same hydrothermal reaction condition as described for Fe−Co MOC.

Fe−Co−P Catalyst Synthesis. Fe−Co MOC powder was placed into a tube furnace, then heated up to 500 °C with 2 °C/min, and held

DOI: 10.1021/acsnano.7b04646
ACS Nano XXXX, XXX, XXX−XXX

for 1 h in Ar to achieve the Fe/Co/C catalyst. For the phosphidation process, 50 mg of Fe/Co/C catalyst was placed behind 1 g of $NaH_2PO_2 \cdot H_2O$ in the gas input direction with 100 sccm Ar flow, then heated up to 350 or 400 °C with 5 °C/min, and kept for 1 h. After phosphidation, the resulting catalyst was collected until the furnace was cooled to room temperature.

Electrochemical Test. The catalyst was dispersed in an ethanol/Nafion solution (v/v = 1/1) at a concentration of 4 mg/mL under 30 min ultrasonication. Then, the catalyst ink was deposited onto a rotating disk electrode using an in-house built spin-coating device at a rotational speed of approximately 400 rpm under a gentle hot air flow. The diameter of the rotating disk electrode is 5 mm, and the mass loading of the catalyst is 0.2 mg/cm^2. Electrochemical tests were performed in 1 M N_2-saturated KOH with a three-electrode system; a rotating disk glassy carbon electrode coated with catalyst was used as a working electrode. Pt wire and Ag/AgCl were employed as counter and reference electrodes. For the positive LSV scan, the scan range was set between 0.3 and 0.95 V with a scan rate of 5 mV/s and a rotating speed of 1600 rpm.

X-ray Absorption Test. *In situ* X-ray absorption spectroscopy measurements at the Fe K-edge (7112 eV) and Co K-edge (7709 eV) on the Fe−Co−P catalysts before and after the OER reaction were made at the 10-BM bending magnet beamline of the Materials Research Collaborative Access Team (MRCAT) at the Advanced Photon Source (APS), Argonne National Laboratory. Measurements were taken in transmission mode. An iron or cobalt foil spectrum was acquired through a third ion chamber simultaneously with each measurement for energy calibration. The catalysts were ground into fine powders and diluted with silica (Davisil 646 silical gel from Sigma-Aldrich) before they were pressed into a cylindrical sample holder to form a self-supported wafer. All spectra were obtained at room temperature in air.

DOS Calculation. DFT calculations were conducted using Quantum ESPRESSO software packages.[69] The optimization and properties were calculated using Perdew−Burke−Ernzerhof generalized gradient approximation with projector-augmented wave sets from Pslibrary 0.3.1.[70] The plane wave kinetic energy cutoff values were 60 and 600 Ry for the wave functions and the charge densities, respectively. The properties were calculated after the structures were relaxed. The phosphide was modeled using a 2 × 2 × 2 super cell with a k-point mesh of 1 × 2 × 1. Furthermore, the DOS was plotted with the Fermi energy set as 0 eV.

ASSOCIATED CONTENT

Supporting Information

The Supporting Information is available free of charge on the ACS Publications website at DOI: 10.1021/acsnano.7b04646.

Further details about TGA, Raman, FTIR, XRD, XPS, TEM, and electrochemisty measurements (PDF)

AUTHOR INFORMATION

Corresponding Authors

*E-mail: jeffrey-t-miller@purdue.edu.
*E-mail: zpeng@uakron.edu.
*E-mail: yu.zhu@uakron.edu.

ORCID

Changlin Zhang: 0000-0002-1207-4264
Zhenmeng Peng: 0000-0003-1230-6800
Yu Zhu: 0000-0002-2201-9066

Author Contributions

⊥K.L. and C.Z. contributed equally to this work.

Notes

The authors declare no competing financial interest.

ACKNOWLEDGMENTS

The authors thank Dr. B. Wang for help with the SEM, Dr. M. Gao for help of HRTEM, and E. Laughlin for technical support. The TEM and SEM observations using FEI Tecnai F20 and Quanta450 were carried out at the Liquid Crystal Institute Characterization Facility of Kent State University. K.L., Y.S., F.Z., H.Z., C.T., and Y.Z. thank the support from the National Science Foundation (NSF) through NSF-CBET 1505943 and 1336057, ACS Petroleum Research Fund (PRF# 53560-DNI 10), and Ohio Federal Network Research (OFRN) of the Center of Excellence. Use of the Advanced Photon Source is supported by the U.S. Department of Energy, Office of Science, and Office of Basic Energy Sciences, under Contract DE-AC02-06CH11357. MRCAT operations are supported by the Department of Energy and the MRCAT member institutions.

REFERENCES

(1) Cook, T. R.; Dogutan, D. K.; Reece, S. Y.; Surendranath, Y.; Teets, T. S.; Nocera, D. G. Solar Energy Supply and Storage for the Legacy and Nonlegacy Worlds. *Chem. Rev.* **2010**, *110*, 6474−6502.

(2) Walter, M. G.; Warren, E. L.; McKone, J. R.; Boettcher, S. W.; Mi, Q.; Santori, E. A.; Lewis, N. S. Solar Water Splitting Cells. *Chem. Rev.* **2010**, *110*, 6446−6473.

(3) Gray, H. B. Powering the Planet with Solar Fuel. *Nat. Chem.* **2009**, *1*, 7−7.

(4) Cheng, F.; Chen, J. Metal-Air Batteries: From Oxygen Reduction Electrochemistry to Cathode Catalysts. *Chem. Soc. Rev.* **2012**, *41*, 2172−2192.

(5) Lewis, N. S.; Nocera, D. G. Powering the Planet: Chemical Challenges in Solar Energy Utilization. *Proc. Natl. Acad. Sci. U. S. A.* **2006**, *103*, 15729−35.

(6) Nocera, D. G. The Artificial Leaf. *Acc. Chem. Res.* **2012**, *45*, 767−776.

(7) Turner, J. A. Sustainable Hydrogen Production. *Science* **2004**, *305*, 972.

(8) Hong, W. T.; Risch, M.; Stoerzinger, K. A.; Grimaud, A.; Suntivich, J.; Shao-Horn, Y. Toward the Rational Design of Non-precious Transition Metal Oxides for Oxygen Electrocatalysis. *Energy Environ. Sci.* **2015**, *8*, 1404−1427.

(9) Chen, D.; Chen, C.; Baiyee, Z. M.; Shao, Z.; Ciucci, F. Nonstoichiometric Oxides as Low-Cost and Highly-Efficient Oxygen Reduction/Evolution Catalysts for Low-Temperature Electrochemical Devices. *Chem. Rev.* **2015**, *115*, 9869−9921.

(10) Tsuji, E.; Imanishi, A.; Fukui, K.-i.; Nakato, Y. Electrocatalytic Activity of Amorphous RuO_2 Electrode for Oxygen Evolution in An Aqueous Solution. *Electrochim. Acta* **2011**, *56*, 2009−2016.

(11) Hu, J.-M.; Zhang, J.-Q.; Cao, C.-N. Oxygen Evolution Reaction on IrO_2-Based DSA® Type Electrodes: Kinetics Analysis of Tafel Lines and EIS. *Int. J. Hydrogen Energy* **2004**, *29*, 791−797.

(12) McCrory, C. C. L.; Jung, S.; Peters, J. C.; Jaramillo, T. F. Benchmarking Heterogeneous Electrocatalysts for the Oxygen Evolution Reaction. *J. Am. Chem. Soc.* **2013**, *135*, 16977−16987.

(13) Li, X.; Hao, X.; Abudula, A.; Guan, G. Nanostructured Catalysts for Electrochemical Water Splitting: Current State and Prospects. *J. Mater. Chem. A* **2016**, *4*, 11973−12000.

(14) Jiao, Y.; Zheng, Y.; Jaroniec, M.; Qiao, S. Z. Design of Electrocatalysts for Oxygen- and Hydrogen-Involving Energy Conversion Reactions. *Chem. Soc. Rev.* **2015**, *44*, 2060−2086.

(15) Zhang, C.; Wang, B.; Shen, X.; Liu, J.; Kong, X.; Chuang, S. S. C.; Yang, D.; Dong, A.; Peng, Z. A Nitrogen-Doped Ordered Mesoporous Carbon/Graphene Framework as Bifunctional Electrocatalyst for Oxygen Reduction and Evolution Reactions. *Nano Energy* **2016**, *30*, 503−510.

(16) Kong, X.; Zhang, C.; Hwang, S. Y.; Chen, Q.; Peng, Z. Free-Standing Holey $Ni(OH)_2$ Nanosheets with Enhanced Activity for Water Oxidation. *Small* **2017**, *13*, 1700334.

DOI: 10.1021/acsnano.7b04646
ACS Nano XXXX, XXX, XXX−XXX

(17) Fang, Z.; Peng, L.; Lv, H.; Zhu, Y.; Yan, C.; Wang, S.; Kalyani, P.; Wu, X.; Yu, G. Metallic Transition Metal Selenide Holey Nanosheets for Efficient Oxygen Evolution Electrocatalysis. *ACS Nano* **2017**, *11*, 9550−9557.

(18) Roger, I.; Shipman, M. A.; Symes, M. D. Earth-Abundant Catalysts for Electrochemical and Photoelectrochemical Water Splitting. *Nat. Rev. Chem.* **2017**, *1*, 0003.

(19) Zhao, S.; Wang, Y.; Dong, J.; He, C.-T.; Yin, H.; An, P.; Zhao, K.; Zhang, X.; Gao, C.; Zhang, L.; Lv, J.; Wang, J.; Zhang, J.; Khattak, A. M.; Khan, N. A.; Wei, Z.; Zhang, J.; Liu, S.; Zhao, H.; Tang, Z. Ultrathin Metal−Organic Framework Nanosheets for Electrocatalytic Oxygen Evolution. *Nat. Energy* **2016**, *1*, 16184.

(20) Bergmann, A.; Martinez-Moreno, E.; Teschner, D.; Chernev, P.; Gliech, M.; de Araújo, J. F.; Reier, T.; Dau, H.; Strasser, P. Reversible Amorphization and the Catalytically Active State of Crystalline Co_3O_4 During Oxygen Evolution. *Nat. Commun.* **2015**, *6*, 8625.

(21) Ganassin, A.; Maljusch, A.; Colic, V.; Spanier, L.; Brandl, K.; Schuhmann, W.; Bandarenka, A. Benchmarking the Performance of Thin-Film Oxide Electrocatalysts for Gas Evolution Reactions at High Current Densities. *ACS Catal.* **2016**, *6*, 3017−3024.

(22) Tae, E. L.; Song, J.; Lee, A. R.; Kim, C. H.; Yoon, S.; Hwang, I. C.; Kim, M. G.; Yoon, K. B. Cobalt Oxide Electrode Doped with Iridium Oxide as Highly Efficient Water Oxidation Electrode. *ACS Catal.* **2015**, *5*, 5525−5529.

(23) Wang, J.; Cui, W.; Liu, Q.; Xing, Z.; Asiri, A. M.; Sun, X. Recent Progress in Cobalt-Based Heterogeneous Catalysts for Electrochemical Water Splitting. *Adv. Mater.* **2016**, *28*, 215−230.

(24) Huynh, M.; Shi, C.; Billinge, S. J. L.; Nocera, D. G. Nature of Activated Manganese Oxide for Oxygen Evolution. *J. Am. Chem. Soc.* **2015**, *137*, 14887−14904.

(25) Meng, Y.; Song, W.; Huang, H.; Ren, Z.; Chen, S.-Y.; Suib, S. L. Structure−Property Relationship of Bifunctional MnO_2 Nanostructures: Highly Efficient, Ultra-Stable Electrochemical Water Oxidation and Oxygen Reduction Reaction Catalysts Identified in Alkaline Media. *J. Am. Chem. Soc.* **2014**, *136*, 11452−11464.

(26) Sun, W.; Cao, L.-m.; Yang, J. Conversion of Inert Cryptomelane-Type Manganese Oxide into a Highly Efficient Oxygen Evolution Catalyst *via* Limited Ir Doping. *J. Mater. Chem. A* **2016**, *4*, 12561−12570.

(27) Gerken, J. B.; Shaner, S. E.; Masse, R. C.; Porubsky, N. J.; Stahl, S. S. A Survey of Diverse Earth Abundant Oxygen Evolution Electrocatalysts Showing Enhanced Activity from Ni-Fe Oxides Containing a Third Metal. *Energy Environ. Sci.* **2014**, *7*, 2376−2382.

(28) Han, L.; Yu, X.-Y.; Lou, X. W. Formation of Prussian-Blue-Analog Nanocages *via* a Direct Etching Method and Their Conversion into Ni−Co-Mixed Oxide for Enhanced Oxygen Evolution. *Adv. Mater.* **2016**, *28*, 4601−4605.

(29) Yang, Y.; Fei, H.; Ruan, G.; Xiang, C.; Tour, J. M. Efficient Electrocatalytic Oxygen Evolution on Amorphous Nickel−Cobalt Binary Oxide Nanoporous Layers. *ACS Nano* **2014**, *8*, 9518−9523.

(30) Bates, M. K.; Jia, Q.; Doan, H.; Liang, W.; Mukerjee, S. Charge-Transfer Rffects in Ni−Fe and Ni−Fe−Co Mixed-Metal Oxides for the Alkaline Oxygen Evolution Reaction. *ACS Catal.* **2016**, *6*, 155−161.

(31) Rios, E.; Gautier, J. L.; Poillerat, G.; Chartier, P. Mixed Valency Spinel Oxides of Transition Metals and Electrocatalysis: Case of the $Mn_xCo_{3-x}O_4$ System. *Electrochim. Acta* **1998**, *44*, 1491−1497.

(32) Chen, L.; Dong, X.; Wang, Y.; Xia, Y. Separating Hydrogen and Oxygen Evolution in Alkaline Water Electrolysis Using Nickel Hydroxide. *Nat. Commun.* **2016**, *7*, 11741.

(33) Liang, H.; Meng, F.; Cabán-Acevedo, M.; Li, L.; Forticaux, A.; Xiu, L.; Wang, Z.; Jin, S. Hydrothermal Continuous Flow Synthesis and Exfoliation of NiCo Layered Double Hydroxide Nanosheets for Enhanced Oxygen Evolution Catalysis. *Nano Lett.* **2015**, *15*, 1421−1427.

(34) Dong, C.; Yuan, X.; Wang, X.; Liu, X.; Dong, W.; Wang, R.; Duan, Y.; Huang, F. Rational Design of Cobalt-Chromium Layered Double Hydroxide as a Highly Efficient Electrocatalyst for Water Oxidation. *J. Mater. Chem. A* **2016**, *4*, 11292−11298.

(35) Fan, K.; Chen, H.; Ji, Y.; Huang, H.; Claesson, P. M.; Daniel, Q.; Philippe, B.; Rensmo, H.; Li, F.; Luo, Y.; Sun, L. Nickel−Vanadium Monolayer Double Hydroxide for Efficient Electrochemical Water Oxidation. *Nat. Commun.* **2016**, *7*, 11981.

(36) Huang, J.; Chen, J.; Yao, T.; He, J.; Jiang, S.; Sun, Z.; Liu, Q.; Cheng, W.; Hu, F.; Jiang, Y.; Pan, Z.; Wei, S. CoOOH Nanosheets with High Mass Activity for Water Oxidation. *Angew. Chem., Int. Ed.* **2015**, *54*, 8722−8727.

(37) Diaz-Morales, O.; Ledezma-Yanez, I.; Koper, M. T. M.; Calle-Vallejo, F. Guidelines for the Rational Design of Ni-Based Double Hydroxide Electrocatalysts for the Oxygen Evolution Reaction. *ACS Catal.* **2015**, *5*, 5380−5387.

(38) Louie, M. W.; Bell, A. T. An Investigation of Thin-Film Ni−Fe Oxide Catalysts for the Electrochemical Evolution of Oxygen. *J. Am. Chem. Soc.* **2013**, *135*, 12329−12337.

(39) Matsumoto, Y.; Sato, E. Electrocatalytic Properties of Transition Metal Oxides for Oxygen Evolution Reaction. *Mater. Chem. Phys.* **1986**, *14*, 397−426.

(40) Yeo, B. S.; Bell, A. T. Enhanced Activity of Gold-Supported Cobalt Oxide for the Electrochemical Evolution of Oxygen. *J. Am. Chem. Soc.* **2011**, *133*, 5587−5593.

(41) Liang, Y.; Li, Y.; Wang, H.; Zhou, J.; Wang, J.; Regier, T.; Dai, H. Co_3O_4 Nanocrystals on Graphene as a Synergistic Catalyst for Oxygen Reduction Reaction. *Nat. Mater.* **2011**, *10*, 780−786.

(42) Fan, X.; Peng, Z.; Ye, R.; Zhou, H.; Guo, X. M_3C (M: Fe, Co, Ni) Nanocrystals Encased in Graphene Nanoribbons: An Active and Stable Bifunctional Electrocatalyst for Oxygen Reduction and Hydrogen Evolution Reactions. *ACS Nano* **2015**, *9*, 7407−7418.

(43) Liu, Y.; Li, J.; Li, F.; Li, W.; Yang, H.; Zhang, X.; Liu, Y.; Ma, J. A Facile Preparation of $CoFe_2O_4$ Nanoparticles on Polyaniline-Functionalised Carbon Nanotubes as Enhanced Catalysts for the Oxygen Evolution Reaction. *J. Mater. Chem. A* **2016**, *4*, 4472−4478.

(44) Lu, X.; Yim, W.-L.; Suryanto, B. H. R.; Zhao, C. Electrocatalytic Oxygen Evolution at Surface-Oxidized Multiwall Carbon Nanotubes. *J. Am. Chem. Soc.* **2015**, *137*, 2901−2907.

(45) Lin, X.; Li, X.; Li, F.; Fang, Y.; Tian, M.; An, X.; Fu, Y.; Jin, J.; Ma, J. Precious-Metal-free Co-Fe-O_x Coupled Nitrogen-Enriched Porous Carbon Nanosheets Derived from Schiff-Base Porous Polymers as Superior Electrocatalysts for the Oxygen Evolution Reaction. *J. Mater. Chem. A* **2016**, *4*, 6505−6512.

(46) Wang, J.; Zhong, H.-x.; Wang, Z.-l.; Meng, F.-l.; Zhang, X.-b. Integrated Three-Dimensional Carbon Paper/Carbon Tubes/Cobalt-Sulfide Sheets as an Efficient Electrode for Overall Water Splitting. *ACS Nano* **2016**, *10*, 2342−2348.

(47) Xu, K.; Chen, P.; Li, X.; Tong, Y.; Ding, H.; Wu, X.; Chu, W.; Peng, Z.; Wu, C.; Xie, Y. Metallic Nickel Nitride Nanosheets Realizing Enhanced Electrochemical Water Oxidation. *J. Am. Chem. Soc.* **2015**, *137*, 4119−4125.

(48) Dutta, A.; Pradhan, N. Developments of Metal Phosphides as Efficient OER Precatalysts. *J. Phys. Chem. Lett.* **2017**, *8*, 144−152.

(49) Stern, L.-A.; Feng, L.; Song, F.; Hu, X. Ni_2P as a Janus Catalyst for Water Splitting: the Oxygen Evolution Activity of Ni_2P Nanoparticles. *Energy Environ. Sci.* **2015**, *8*, 2347−2351.

(50) Li, J.; Li, J.; Zhou, X.; Xia, Z.; Gao, W.; Ma, Y.; Qu, Y. Highly Efficient and Robust Nickel Phosphides as Bifunctional Electrocatalysts for Overall Water-Splitting. *ACS Appl. Mater. Interfaces* **2016**, *8*, 10826−10834.

(51) Jiang, N.; You, B.; Sheng, M.; Sun, Y. Bifunctionality and Mechanism of Electrodeposited Nickel−Phosphorous Films for Efficient Overall Water Splitting. *ChemCatChem* **2016**, *8*, 106−112.

(52) Tian, J.; Liu, Q.; Asiri, A. M.; Sun, X. Self-Supported Nanoporous Cobalt Phosphide Nanowire Arrays: An Efficient 3D Hydrogen-Evolving Cathode over the Wide Range of pH 0−14. *J. Am. Chem. Soc.* **2014**, *136*, 7587−7590.

(53) Zou, F.; Chen, Y.-M.; Liu, K.; Yu, Z.; Liang, W.; Bhaway, S. M.; Gao, M.; Zhu, Y. Metal Organic Frameworks Derived Hierarchical Hollow NiO/Ni/Graphene Composites for Lithium and Sodium Storage. *ACS Nano* **2016**, *10*, 377−386.

DOI: 10.1021/acsnano.7b04646
ACS Nano XXXX, XXX, XXX−XXX

(54) Denton, A. R.; Ashcroft, N. W. Vegard's Law. *Phys. Rev. A: At., Mol., Opt. Phys.* **1991**, *43*, 3161−3164.
(55) Shinagawa, T.; Garcia-Esparza, A. T.; Takanabe, K. Insight on Tafel Slopes from a Microkinetic Analysis of Aqueous Electrocatalysis for Energy Conversion. *Sci. Rep.* **2015**, *5*, 13801.
(56) Burke, M. S.; Kast, M. G.; Trotochaud, L.; Smith, A. M.; Boettcher, S. W. Cobalt−Iron (Oxy)hydroxide Oxygen Evolution Electrocatalysts: The Role of Structure and Composition on Activity, Stability, and Mechanism. *J. Am. Chem. Soc.* **2015**, *137*, 3638−3648.
(57) Jain, A.; Ong, S. P.; Hautier, G.; Chen, W.; Richards, W. D.; Dacek, S.; Cholia, S.; Gunter, D.; Skinner, D.; Ceder, G.; Persson, K. A. Commentary: The Materials Project: A Materials Genome Approach to Accelerating Materials Innovation. *APL Mater.* **2013**, *1*, 011002.
(58) Zhang, Z.; Lu, B.; Hao, J.; Yang, W.; Tang, J. FeP Nanoparticles Grown on Graphene Sheets as Highly Active Non-Precious-Metal Electrocatalysts For Hydrogen Evolution Reaction. *Chem. Commun.* **2014**, *50*, 11554−11557.
(59) Zhu, X.; Liu, M.; Liu, Y.; Chen, R.; Nie, Z.; Li, J.; Yao, S. Carbon-Coated Hollow Mesoporous FeP Microcubes: An Efficient and Stable Electrocatalyst for Hydrogen Evolution. *J. Mater. Chem. A* **2016**, *4*, 8974−8977.
(60) Hao, J.; Yang, W.; Zhang, Z.; Tang, J. Metal-Organic Frameworks Derived $Co_xFe_{1-x}P$ Nanocubes for Electrochemical Hydrogen Evolution. *Nanoscale* **2015**, *7*, 11055−62.
(61) Cecilia, J. A.; Infantes-Molina, A.; Rodríguez-Castellón, E.; Jiménez-López, A. Dibenzothiophene Hydrodesulfurization over Cobalt Phosphide Catalysts Prepared Through a New Synthetic Approach: Effect of the Support. *Appl. Catal., B* **2009**, *92*, 100−113.
(62) Abdel-Samad, H.; Watson, P. R. An XPS Study of the Adsorption of Lead on Goethite (α-FeOOH). *Appl. Surf. Sci.* **1998**, *136*, 46−54.
(63) Baltrusaitis, J.; Cwiertny, D. M.; Grassian, V. H. Adsorption of Sulfur Dioxide on Hematite and Goethite Particle Surfaces. *Phys. Chem. Chem. Phys.* **2007**, *9*, 5542−5554.
(64) Friebel, D.; Louie, M. W.; Bajdich, M.; Sanwald, K. E.; Cai, Y.; Wise, A. M.; Cheng, M.-J.; Sokaras, D.; Weng, T.-C.; Alonso-Mori, R.; Davis, R. C.; Bargar, J. R.; Nørskov, J. K.; Nilsson, A.; Bell, A. T. Identification of Highly Active Fe Sites in (Ni,Fe)OOH for Electrocatalytic Water Splitting. *J. Am. Chem. Soc.* **2015**, *137*, 1305−1313.
(65) Ahn, H. S.; Bard, A. J. Surface Interrogation Scanning Electrochemical Microscopy of $Ni_{1-x}Fe_xOOH$ ($0 < x < 0.27$) Oxygen Evolving Catalyst: Kinetics of the "Fast" Iron Sites. *J. Am. Chem. Soc.* **2016**, *138*, 313−318.
(66) Zhang, B.; Zheng, X.; Voznyy, O.; Comin, R.; Bajdich, M.; García-Melchor, M.; Han, L.; Xu, J.; Liu, M.; Zheng, L.; García de Arquer, F. P.; Dinh, C. T.; Fan, F.; Yuan, M.; Yassitepe, E.; Chen, N.; Regier, T.; Liu, P.; Li, Y.; De Luna, P.; et al. Homogeneously Dispersed Multimetal Oxygen-Evolving Catalysts. *Science* **2016**, *352*, 333−337.
(67) Zhong, H.; Wang, J.; Meng, F.; Zhang, X. *In Situ* Activating Ubiquitous Rust towards Low-Cost, Efficient, Free-Standing, and Recoverable Oxygen Evolution Electrodes. *Angew. Chem., Int. Ed.* **2016**, *55*, 9937−9941.
(68) Morales-Guio, C. G.; Liardet, L.; Hu, X. Oxidatively Electrodeposited Thin-Film Transition Metal (Oxy)hydroxides as Oxygen Evolution Catalysts. *J. Am. Chem. Soc.* **2016**, *138*, 8946−8957.
(69) Giannozzi, P.; Baroni, S.; Bonini, N.; Calandra, M.; Car, R.; Cavazzoni, C.; Ceresoli, D.; Chiarotti, G. L.; Cococcioni, M.; Dabo, I.; et al. A Modular and Open-Source Software Project for Quantum Simulations of Materials. *J. Phys.: Condens. Matter* **2009**, *21*, 395502.
(70) Kucukbenli, E.; Monni, M.; Adetunji, B. I.; Ge, X.; Adebayo, G. A.; Marzari, N.; de Gironcoli, S.; Dal Corso, A. Projector Augmented-Wave and All-Electron Calculations Across the Periodic Table: A Comparison of Structural and Energetic Properties. *arxiv.org/abs/1404.3015*, **2014**.

DOI: 10.1021/acsnano.7b04646
ACS Nano XXXX, XXX, XXX−XXX